

1 Automated Quantification of the Impact of the Wood-
2 decay fungus *Physisporinus vitreus* on the Cell Wall
3 Structure of Norway spruce by Tomographic Microscopy

4
5 M. J. Fuhr^{a,b}, C. Stührk^{a,b}, B. Münch^c, F. W. M. R. Schwarze^b and M. Schubert^b

6 ^a*ETH Zurich, Institute for Building Materials, Computational Physics for Engineering*
7 *Materials, Schafmattstrasse 6, HIF E18, CH-8093 Zurich, Switzerland*

8 ^b*EMPA, Swiss Federal Laboratories for Materials Science and Technology, Wood*
9 *Laboratory, Group of Wood Protection and Biotechnology, Lerchenfeldstrasse 5, CH-9014 St*
10 *Gallen, Switzerland*

11 ^c*EMPA, Swiss Federal Laboratories for Materials Science and Technology, Group*
12 *Concrete Technology, CH-8600 Dübendorf, Switzerland*

13
14 Corresponding author: M.J. Fuhr. Phone: +41 44 633 7153

15
16 Email addresses: MF: mfuhr@ethz.ch
17 CS: Chris.Stuehrk@empa.ch
18 BM: Beat.Muench@empa.ch
19 FS: Francis.Schwarze@empa.ch
20 MS: Mark.Schubert@empa.ch

21

22 4 figures

23 4372 words

24

25 **Abstract**

26 Wood-decay fungi decompose their substrate by extracellular, degradative enzymes and play an
27 important role in natural ecosystems by recycling carbon and minerals fixed in plants. Thereby,
28 they cause significant damage to the wood structure and limit the use of wood as building
29 material. Besides their role as biodeteriorators wood-decay fungi can be used for
30 biotechnological purposes, e.g. the white-rot fungus *Physisporinus vitreus* for improving the
31 uptake of preservatives and wood-modification substances of refractory wood. Therefore, the
32 visualization and the quantification of microscopic decay patterns are important for the study of
33 the impact of wood-decay fungi in general, as well as for wood-decay fungi and microorganisms
34 with possible applications in biotechnology. In the present work, we developed a method for the
35 automated localization and quantification of microscopic cell wall elements (CWE) of Norway
36 spruce wood such as bordered pits, intrinsic defects, hyphae or alterations induced by *P. vitreus*
37 using high resolution X-ray computed tomographic microscopy. In addition to classical
38 destructive wood anatomical methods such as light or laser scanning microscopy, our method
39 allows for the first time to compute the properties (e.g. area, orientation and size-distribution) of
40 CWE of the tracheids in a sample. This is essential for modeling the influence of microscopic
41 CWE to macroscopic properties such as wood strength and permeability.

42

43 **Keywords (max 6 words)**

44 Image Analysis, Bordered Pits, Segmentation, Synchrotron X-ray tomography microscopy
45 (SRXTM), Phase-contrast, *Picea abies*

46

47 **1. Introduction**

48 Wood-decay fungi degrade their substrate, a complex anisotropic material featuring several
49 hierarchical levels of organization from macroscopic (e.g. growth ring) over the mesoscopic (e.g.
50 set of wood cells) down to the microscopic and nanoscopic scale (e.g. wood cells and fibrils), by
51 extracellular, degradative enzymes. They play an important role in natural ecosystems by
52 recycling carbon and minerals fixed in plants. Thereby, they cause a significant damage to the
53 wood structure and limit the possible use of wood as building material. Besides their role as
54 biodeteriorators wood-decay fungi can be used for biotechnological applications.

55 Recent investigations have shown that wood-decay fungi have many valuable
56 biotechnological purposes in the pure and applied wood sciences (Mai et al., 2004; Messner et
57 al., 2002; Schwarze, 2008). Alterations in the cell wall structure and/or the distribution of the cell
58 wall constituents are reflected in the plasticity of the wood degradation modes of different fungi
59 (Deflorio et al., 2005; Schwarze, 2008). The specificity of their enzymes and the mild conditions
60 under which degradation proceeds potentially make them suitable agents for wood modification
61 such as biopulping, bioremediation or bioincising (Majcherczyk and Hüttermann, 1988;
62 Messner et al., 2002; Schwarze, 2009).

63 The biotechnological process of bioincising is a promising approach for improving the
64 uptake of preservatives and wood-modification substances by refractory wood due to
65 degradation of bordered pits by the white-rot fungus *Physisporinus vitreus* (Pers.: Fr.) P. Karst.
66 (Schwarze and Landmesser, 2000; Schwarze et al., 2006). Furthermore because of its exceptional

67 pattern of degradation, *P. vitreus* is successfully used to improve the acoustic properties of the
68 tonewood of Norway spruce wood (*Picea abies* L.) used for music instruments by selectively
69 delignifying the secondary walls without affecting the middle lamellae, even at advanced stages
70 (Schwarze et al., 2008; Spycher et al., 2008). However, a successful up-scaling of
71 biotechnological processes in which *P. vitreus* is used to improve substrate properties requires a
72 set of investigations for the identification and detection of important growth parameters
73 (Schubert and Schwarze, 2010; Schubert et al., 2010; Schubert et al., 2009) and the elucidation
74 of the wood - fungus interactions (Lehringer et al., 2010). Hence, the visualization and
75 quantification of microscopic decay patterns are of interest for the study of wood-decay fungi in
76 general as well as for wood-decay fungi and microorganisms with possible applications for
77 biotechnology. However, the quantification of microscopic cell wall alterations (e.g. their size-
78 distribution in space and time) is difficult, because of the opacity of wood and the heterogeneity
79 of its structure.

80 Classical destructive methods for analyzing wood-decay fungi include light and electron
81 microscopy of thin microtome sections. The advantages of the latter methods are the elucidation
82 and interpretation of wood-decay patterns with the help of specific staining techniques
83 (Schwarze, 2007). However, classical microscopy techniques only provide two-dimensional (2D)
84 information and do not allow the quantification of alterations in the cell wall structure. Yet, the
85 growth of fungi in wood is a complex three-dimensional (3D) process due to the diverse
86 alignment of wood cells and the distribution of nutrients. In order to successfully model the
87 growth and impact of wood-decay fungi, more quantitative information on the distribution of
88 fungal activity at the microscopic level in space and time is required (Fuhr et al., 2010).

89 At the microscopic scale, non-destructive techniques based on X-ray computed
90 tomographic (XCT) microscopy have been mostly used in wood research for 3D investigation of
91 mycelial expansion and the impact of wood-decay fungi. In XCT, the beam attenuation is
92 acquired either by absorption or by scattering, according to the atomic number of the constituents
93 at each volume element (voxel). The 2D projections are subsequently reconstructed into a 3D
94 attenuation map. McGovern (McGovern et al., 2010) measured the mass loss of wood specimens
95 using XCT with a voxel size of approximately 0.34 mm³. Illman and Dowd (1999) and Van den
96 Bulcke et al. (2009) analyzed the density and structure of incubated wood applying high-
97 resolution XCT microscopy. Van den Bulcke et al. (2008) identified single hypha of
98 *Aureobasidium pullulans* with a diameter of approximately 10 µm in wood using high-resolution
99 XCT microscopy. However an automated separation of fungus and wood was not accomplished.
100 It seems that confocal laser scanning microscopy (CLSM) is the appropriate technique to analyze
101 the 3D structure of mycelium in wood, because of the capacity to separate fluorescence-stained
102 fungi from the wood substrate during measurement (Dickson and Kolesik, 1999; Stührk et al.,
103 2010). However, the penetration depth of the laser light into wood is limited and the cell wall
104 damages are not clearly visible, because of the weak autofluorescence of wood. Therefore, we
105 suggest the use of high-resolution XCT microscopy for analyzing the impact of wood-decay
106 fungi.

107 To the best of our knowledge, the present work describes for the first time a computer
108 based automated procedure for the localization and quantification of cell wall elements (CWE)
109 such as bordered pits, intrinsic defects and alterations induced by *P. vitreus* by means of high-
110 resolution XCT microscopy. The quantitative information arising from this procedure allows to
111 e.g. analyze the distribution of the fungal activity of *P. vitreus* in the late- and early wood of

112 Norway spruce depending on the incubation conditions, which is essential for the successful
113 manufacture of fungal modified wood.

114

115 **2. Materials and methods**

116 2.1 Wood and fungus

117 We use defect-free heartwood wood from a Norway spruce tree (*Picea abies* [L.] Karst.), grown
118 in Switzerland. The three alignments of wood cells are longitudinal (parallel to the fibre), radial
119 (perpendicular to the fibre) and tangential (parallel to the growth rings). There are mainly two
120 types of cells in softwoods, tracheids and rays. The cell walls of tracheids consist of several
121 layers denoted as secondary wall S₁, S₂, S₃ and primary wall (PW) from the lumen (i.e. voids
122 within the cells) to the middle lamella (ML) forming the border of two adjacent tracheids. In
123 order to transport water and nutrients in longitudinal and radial direction, the cell lumina are
124 connected via bordered and simple pits.

125 Specimens with dimensions of approximately 400 µm (radial) × 10 mm (tangential) × 6
126 mm (longitudinal) were produced with a microtome. All specimen faces, except the radial ones,
127 were subsequently coated by brushing (Nuvovern ACR Emaillack, Walter Mäder AG,
128 Killwangen, Switzerland). After 24h, the procedure was repeated to guarantee a solid sealing.
129 Subsequently, the specimens were conditioned for two weeks at 22°C and 50% relative humidity
130 (RH). Thereafter, the specimens were sterilized with hot steam (121°C, 20 min and 2 bar) and
131 placed on a 'feeder block' of Scots pines (*Pinus sylvestris*) previously colonized with the white-
132 rot basidiomycete *Physisporinus vitreus* Empa strain 642. Specimens were incubated under
133 sterile conditions for seven weeks at 22°C and 70% RH. After incubation, the specimens were

134 cut into elongated wood prisms of approximately $400\ \mu\text{m}$ (radial) \times $400\ \text{mm}$ (tangential) \times $6\ \text{mm}$
135 (longitudinal) using a microtome.

136 For the tomographic experiments, the samples were glued onto cylindrical sample holders
137 using double-side adhesive tape, the longitudinal axis of the sample being located at the rotation
138 axis of the tomographic stage.

139

140 2.2 Synchrotron Tomographic Microscopy

141 Synchrotron radiation facilities provide photon beams of energy densities that outrange
142 conventional X-ray sources by orders of magnitude. Among other benefits, the high brilliance
143 and brightness of synchrotron based X-rays enable tomographic microscopy at sub-micrometer
144 scale.

145 In the present study, tomographic experiments were performed at the TOMCAT beam
146 line (Tomographic Microscopy and Coherent Radiology experiments) at the synchrotron
147 radiation facility Swiss Light Source (SLS) at the Paul Scherrer Institute (PSI) in Villigen
148 (Switzerland). The TOMCAT beam line operates in both, absorption and phase-contrast mode.
149 Phase-contrast tomography analyzes the Zernike phase-contrasts of the X-ray beam induced by
150 refraction (Neuhäusler et al., 2003) and is preferable for materials with low absorption contrast
151 such as wood. Trtik (Trtik et al., 2007) and Mannes (Mannes et al., 2010) demonstrated the use
152 of phase-contrast tomography for the analysis of 3D structures in Norway spruce wood down to
153 the microscopic level.

154 In order to minimize dehydration of the specimen during measurements a climatic
155 chamber to control the air humidity at 95% RH (Derome et al., 2010) was used. The temperature
156 remained constant during measurements at 25°C . For each specimen, a set of 1501 projections

157 over 180° was acquired with a photon energy of 9.9 and 20.2 keV for absorption or phase-
158 contrast mode, respectively. The X-rays were converted into visible light by a YAG:Ce $20\ \mu\text{m}$
159 scintillator and projected to a charge coupled device (CCD) featuring a resolution of $2048 \times$
160 2048 pixels and a dynamic range of 14-bit. The nominal edge length of the cubic voxels was
161 $0.37\ \mu\text{m}$ by using an optical objective with the magnification ($20\times$) and a field of view of $0.75 \times$
162 $0.75\ \text{mm}$. The total scanning time was approximately 15 minutes for both, absorption and phase-
163 contrast mode. Stampanoni et al. (2006) provides further technical specifications for TOMCAT.

164 The reconstruction of the original projections into a stack of 2048 transverse sections
165 termed tomograms was based on Filtered-Back-Projection by using the Parzen filter supporting
166 noise suppression. The tomograms are 16-bit gray-level TIFF images. The projection values
167 were initially corrected with dark- and flat-field images and the attenuation values thereof were
168 obtained by Lambert-inversion. Stripe artifacts originating from defective detector pixels were
169 eliminated (Munch et al., 2009) and centering artifacts remedied.

170

171 2.3. Analysis of tracheid cell wall elements

172 Fig. 1 illustrates the cell wall analysis process and Fig. 2 presents the core algorithm. The
173 original data, a stack of n subsequent tomograms of the specimen is displayed in Fig. 1a, the data
174 processing yielding the CWE in Figs. 1b - d. Initially, the ROI of each tracheid is manually
175 identified in the 3D tomograms. The 3D tracheid objects are subsequently mapped into 2D by
176 applying a cylindrical projection, each point representing the mean attenuation of the cell wall
177 voxels at an angle α , referring to the centre of gravity of the tracheid. The resulting tracheidal
178 2D-map is a gray-level image of size $n \times s$, where $s \sim 2 \cdot \pi / \alpha$, in which regions of low attenuation

179 values (i.e. CWE) are clearly visible. After segmentation, the distribution of the CWE size and
180 the orientation was determined.

181 First, a region of interest (ROI) was selected and transformed into a binary mask
182 separating air (black pixels) and wood material (white pixels). Segmentation was based on gray-
183 level thresholding using Otsu's method (Otsu, 1979). Fig. 1b shows the original tomograms after
184 applying a morphological closing operation by using a spherical structuring element (SE) with
185 the radius of 3 pixels, in order to remove small objects mainly originating from noise (Gonzalez
186 et al., 2009). The resulting filtered mask is the basis for the segmentation and mapping of the
187 tracheids.

188 Tracheids were segmented by constructing the watersheds between adjacent and closed
189 lumina (Meyer, 1994). Since the lumina might not be closed because of CWE (arrow in Fig. 3a),
190 a morphological closing operation using a SE of $3 \times 3 \times 150$ pixels was applied (Fig. 1c) prior to
191 watershed construction. Subsequently, each spanning cluster is labeled as shown by the colors in
192 Fig. 1c. The obtained label mask of each tomogram makes the segmentation of a tracheid in the
193 filtered mask possible and therefore the construction of a 3D tracheid mask, which is finally used
194 to select and map the cell wall voxels to a tracheidal 2D-map by using a cylindrical projection.
195 Fig. 1d illustrates this process for one of the tomograms.

196

197 **3 Results and Discussion**

198 In order to demonstrate the potential of the method we analyzed single tracheids of a ROI with
199 the size of $125 \times 125 \times 400$ pixels using synchrotron XCT in absorption (Fig. 3a) and phase-
200 contrast mode (Fig. 3b) visualized by isosurfaces in Figs. 3a and b respectively. CWE such as
201 bordered pits (P), intrinsic defects or cell wall alterations induced by *P. vitreus* (F, L) were

202 marked. The tracheidal 2D-map of this tracheid is shown in Fig. 4a. The CWE are clearly visible
203 and their segmentation was possible (Fig. 4b). Fig. 4c shows the histogram of the CWE areas.
204 Their mean attenuation can be interpreted as a measure of cell wall damage as shown in the inset.
205 The results revealed the tracheid's lateral surface of approximately $9800 \mu\text{m}^2$, had a total number
206 of CWE of 18 with an area of approximately $285 \mu\text{m}^2$, which relates to approximately 3% of the
207 tracheid's lateral surface. The largest and the smallest CWE had areas of $72 \mu\text{m}^2$ and $0.05 \mu\text{m}^2$,
208 respectively. Most of the CWE were smaller than $40 \mu\text{m}^2$. In Addition, most CWE occurred in
209 the tangential cell walls (Fig. 4a and b) and different shapes of CWE were recorded in tangential
210 and radial cell walls. Larger CWE showed a lower mean attenuation than smaller CWE.

211 The detection and computing of the CWE revealed clusters of pixels with a very low
212 attenuation as illustrated in the tracheidal 2D-map (Fig. 3b and Fig. 4a). However, the shape of
213 the cell wall and of the 'holes' strongly depends on the constant value for the isosurfaces (Figs.
214 3a and b) and the binary mask of the tracheidal 2D-map (Fig. 4a). Thus, for future measurements
215 it is necessary to compare the tracheids before and after fungal exposure in order to identify
216 alterations of the cell wall accurately. Therefore, the scanning procedure may be time
217 consuming, but recent developments make laboratory-based phase-contrast XCT microscopy
218 available (Mayo et al., 2010).

219 Since tracheids exhibit a complex 3D shape the presented cylindrical projection distorts
220 the cell wall and an elliptic cylindrical map projection might be more adequate. Furthermore,
221 there is more noise in the absorption than in phase-contrast based tomograms, which makes
222 analysis more difficult. Therefore, we suggest using phase-contrast based tomographic
223 microscopy. Nevertheless, the analysis shows pits and cell wall alterations that might be induced
224 by fungal activity, because the pattern of the damages were similar to those found in semi-thin

225 light microscopy sections of incubated wood samples by Lehringer et al. (2010). We found that
226 most of the cell wall alterations were located in the vicinity of bordered pits, and that the size-
227 distribution in Fig. 4c shows a concentration of pixels with low attenuation to large CWE's such
228 as cell wall alterations. This results corresponds with the findings of Lehringer et al. (2010) and
229 according to his classification system we are able to classify the cell wall and bordered pits
230 (indicated by L in Fig. 3a and b) as 'strongly degraded'.

231 Despite the inherent structure of wood, fungi degrade woody tissues, and decay types fall
232 into three categories according to their mode of degradation of the woody cell walls.
233 Traditionally, wood decomposition by fungi is usually classified into three categories based on
234 micro-morphological and chemical characteristics of decay, resulting in different patterns of
235 degradation of the cell wall: soft rot, brown rot and white rot, the latter subdivided into
236 simultaneous rot and selective delignification as caused by e.g. *P. vitreus* (Schwarze 2008).
237 Finally, the presented method has the potential to identify and quantify those cell wall alterations
238 caused by different decay types and additionally other objects within wood such as bordered pits,
239 intrinsic defects or hyphae by comparing the wood sample before and after fungal incubation.

240

241 **4 Conclusion**

242 We presented a method to analyze and quantify microscopic cell wall elements (CWE) such as
243 pits, intrinsic defects and cell wall alterations induced by *Physisporinus vitreus*. Our analysis
244 focused on Norway spruce tracheids degraded by the white-rot fungus *P. vitreus*. The CWE were
245 clearly visible and it was possible to segment and determine the distribution of the CWE size and
246 orientation.

247 We found that the most of the cell wall alterations were located in the vicinity of the
248 bordered pits and the computed size-distribution shows a concentration of pixels with low
249 attenuation to large CWE such as cell wall alterations. However, in addition to this classical
250 wood anatomical method, for the first time our approach allowed to compute the properties (e.g.
251 area, orientation and size-distribution) of cell wall elements of each tracheid of a specimen,
252 which is essential for linking the influence of microscopic cell wall elements to macroscopic
253 system properties such as wood strength or permeability.

254 Therefore, in the future we will systematically measure the fungal activity of *P. vitreus* in
255 Norway spruce samples for different incubation periods and model the evolution of its impact to
256 the cell wall structure. The obtained models are essential to simulate the permeability changes of
257 infected wood in order to optimize the choice of pellet concentration and reaction times that are
258 required to induce a certain degree of wood permeability by *P. vitreus*. Furthermore, the
259 presented method facilitates the development and calibration of mathematical models to optimize
260 the impact of wood decay-fungi for biotechnological applications in pure and applied wood
261 sciences.

262

263 **Acknowledgments**

264 We acknowledge contributions and support of (in alphabetical order), Francois Gagnat, Hans
265 Herrmann, Christian Lehringer, David Mannes, Peter Niemz, Pavel Trtik, and Falk Wittel. We
266 thank to Masuru Abuku and Frederica Marone for their assistance during the measurements and
267 Dominique Derome for supplying the climatic chamber. The authors express their gratitude to
268 the Swiss National Foundation (SNF) No. 205321-121701 for its financial support.

269

270 **Figure captions**

271 Figure 1: Schematic workflow from (a) tomographic experiment to (b-d) quantification of cell
272 wall elements. (a) Acquisition of original data, a stack of n subsequent tomograms, and manual
273 identification of a ROI. (b) Segmentation of the tomograms to a binary mask and removing of
274 artifacts. (c) Closing of the cell lumina in the filtered mask in order to obtain a label mask and a
275 watershed mask to identify the pixels corresponding to a specific tracheid. (d) Construction of
276 the tracheid mask and mapping procedure mapping. The 3D tracheid object is subsequently
277 mapped into 2D by using a cylindrical projection, where each point represents the mean
278 attenuation of the cell wall voxels at an angle α , referring to the centre of gravity of the tracheid.
279 Based on the resulting tracheidal 2D-map, which is a gray-level image of size $n \times s$, it is possible
280 to segment and determine the distribution of the CWE size and orientation.

281 Figure 2: Core algorithm for computing the size-distribution of cell wall elements of a tracheid.

282 Figure 3: ROI with a size of $125 \times 125 \times 400$ pixels of a specimen incubated with *P. vitreus* for 8
283 weeks. The sample was measured by using the synchrotron tomographic microscopy in (a)
284 absorption and (b) phase-contrast mode and visualized by isosurfaces. The clusters of pixels with
285 a very low attenuation indicate cell wall elements (CWE) such as pits (P), intrinsic defects or cell
286 wall alterations may induced by *P. vitreus* (F,L).

287 Figure 4: Quantification of cell wall elements (CWE). (a) Dark colors in the tracheidal 2D-map
288 correspond to a low attenuation of the beam and therefore to a low density of the cell wall. The
289 pits and cell wall alterations induced by the white-rot fungus *P. vitreus* are clearly visible. (b)
290 Identification of the CWE by construction a threshold based binary mask of the tracheidal 2D-
291 map. The tomogram of Fig. 1 corresponds to the marked row (dashed line). (c) An automated

292 segmentation of CWE allows analyzing e.g. their size-distribution. The inset shows the area of
293 the CWE plotted against their mean attenuation.

294

295 **References**

- 296 Deflorio, G., Hein, S., Fink, S., Spiecker, H., Schwarze, F.W.M.R., 2005. The application of
297 wood decay fungi to enhance annual ring detection in three diffuse-porous hardwoods.
298 *Dendrochronologia* 22, 123-130.
- 299 Derome, D., Griffa, M., Koebel, M., Carmeliet, J., 2010. Hysteretic swelling of wood at cellular
300 scale probed by phase-contrast X-ray tomography. *J. Struct. Biol.* 173, 180-190.
- 301 Dickson, S., Kolesik, P., 1999. Visualisation of mycorrhizal fungal structures and quantification
302 of their surface area and volume using laser scanning confocal microscopy. *Mycorrhiza*
303 9, 205-213.
- 304 Fuhr, M.J., Schubert, M., Schwarze, F.W.M.R., Herrmann, H.J., 2010. Modeling hyphal growth
305 of the wood decay fungus *Physisporinus vitreus*. arXiv: 1101.1747.
- 306 Gonzalez, R.C., Woods, R.E., Eddins, S.L., 2009. *Digital Image Processing Using MATLAB.*,
307 second ed., Gatesmark Publishing.
- 308 Illman, B., Dowd, B., 1999. High Resolution Microtomography for Density and Spatial
309 Information about Wood Structures. In: Bonse, U., (Ed.), *Proceedings of SPIE on*
310 *Developments in X-ray Tomography II*. Society of Photo-Optical Instrumentation
311 Engineers, Washington, DC. pp. 198-204.
- 312 Lehringer, C., Hillebrand, K., Richter, K., Arnold, M., Schwarze, F.W.M.R., Militz, H., 2010.
313 Anatomy of bioincised Norway spruce wood. *International Biodeterioration &*
314 *Biodegradation* 64, 346-355.
- 315 Mai, C., Kües, U., Militz, H., 2004. Biotechnology in the wood industry. *Appl. Microbiol.*
316 *Biotechnol.* 63, 477-494.
- 317 Majcherczyk, A., Hüttermann, A., 1988. Bioremediation of wood treated with preservative using
318 white-rot fungi. In: Bruce, A., Palfreyman J.W., (Eds.), *Forest Products Biotechnology*,
319 Taylor and Francis, London. pp. 129-140.

320 Mannes, D., Marone, F., Lehmann, E., Stampanoni, M., Niemz, P., 2010. Application areas of
321 synchrotron radiation tomographic microscopy for wood research. *Wood Sci. Technol.*
322 44, 67-84.

323 Mayo, S.C., Chen, F., Evans, R., 2010. Micron-scale 3D imaging of wood and plant
324 microstructure using high-resolution X-ray phase-contrast microtomography. *J. Struct.*
325 *Biol.* 171, 182-188.

326 McGovern, M., Senalik, A., Chen, G., Beall, F., Reis, H., 2010. Detection and assessment of
327 wood decay using x-ray computer tomography. In: Tomizuka, M., (Ed.), *Sensors and*
328 *Smart Structures Technologies for Civil, Mechanical, and Aerospace Systems 2010.*
329 *Proceedings of the SPIE*, Vol. 7647, San Diego, USA. pp. 76474B-76474B-12.

330 Messner, K., Fackler, K., Lamaipis, P., Gindl, W., Srebotnik, E., Watanabe, T., 2002.
331 Biotechnological wood modification. *Proceedings of the International Symposium on*
332 *Wood-based Materials*, part 2, Vienna University, Vienna. pp. 45-49.

333 Meyer, F., 1994. Topographic distance and watershed lines. *Signal Processing* 38, 113-125.

334 Munch, B., Trtik, P., Marone, F., Stampanoni, M., 2009. Stripe and ring artifact removal with
335 combined wavelet - Fourier filtering. *Optics Express* 17, 8567-8591.

336 Neuhäusler, U., Schneider, G., Ludwig, W., Hambach, D., 2003. Phase contrast X-ray
337 microscopy at 4 keV photon energy with 60nm resolution. *J. Phys. IV France* 104, 567-
338 570.

339 Otsu, N., 1979. A threshold selection method from gray-level histograms. *IEEE Trans. Syst.*
340 *Man. Cyber.* 9, 62-66.

341 Schubert, M., Schwarze, F.W.M.R., 2010. Evaluation of the interspecific competitive ability of
342 the bioincising fungus *Physisporinus vitreus*. *J. Basic Microbiol.* 50, 1-9.

343 Schubert, M., Mourad, S., Schwarze, F.W.M.R., 2010. Radial basis function neural networks for
344 modeling growth rates of the basidiomycetes *Physisporinus vitreus* and *Neolentinus*
345 *lepideus*. *Appl. Microbiol. Biotechnol.* 85, 703-712.

346 Schubert, M., Dengler, V., Mourad S., Schwarze, F.W.M.R., 2009. Determination of optimal
347 growth parameters for the bioincising fungus *Physisporinus vitreus* by means of response
348 surface methodology. *J. Appl. Microbiol.* 106, 1734-1742.

349 Schwarze, F.W.M.R., 2007. Wood decay under the microscope. *Fungal Biol. Rev.* 1, 133-170.

350 Schwarze, F.W.M.R., Schubert, M., 2009. Enhance uptake of wood modification agents in
351 'bioincised' wood. Int. Res. Group Wood Prot. Paper prepared for 40th Annu. Meet.
352 Beijing, China 24–28 May 2009, 1–8.

353 Schwarze, F.W.M.R., 2008. Diagnosis and prognosis of the development of wood decay in urban
354 trees, ENSPEC, Melbourne.

355 Schwarze, F.W.M.R., Landmesser, H., 2000. Preferential degradation of pit membranes within
356 tracheids by the basidiomycete *Physisporinus vitreus*. *Holzforschung* 54, 461-462.

357 Schwarze, F.W.M.R., Spycher, M., Fink, S., 2008. Superior wood for violins - wood decay fungi
358 as a substitute for cold climate. *New Phytol.* 179,1095-1104.

359 Schwarze, F.W.M.R., Landmesser, H., Zraggen, B., Heeb, M., 2006. Permeability changes in
360 heartwood of *Picea abies* and *Abies alba* induced by incubation with *Physisporinus*
361 *vitreus*. *Holzforschung* 60: 450-454.

362 Spycher, M., Schwarze, F.W.M.R., Steiger, R., 2008. Assessment of resonance wood quality by
363 comparing its physical and histological properties. *Wood Sci. Technol.* 42, 325-342.

364 Stampanoni, M., Groso, A., Isenegger, A., Mikuljan, G., Chen, Q., Meister, D., Lange, M.,
365 Betemps, R., Henein, S., Abela, R., 2007. TOMCAT: a beamline for tomographic
366 microscopy and coherent radiology experiments. *Synchrotron Radiat. Instrum.* 879, 848-
367 851.

368 Stührk, C., Fuhr, M., Schubert, M., Schwarze, F.W.M.R., 2010. Analyzing hyphal growth of the
369 bioincising fungus *Physisporinus vitreus* with light-, confocal laser scanning- and,
370 Synchrotron X-ray tomographic microscopy. Paper prepared for the 41st Annual Meeting
371 Biarritz, France.

372 Trtik, P., Dual, J., Keunecke, D., Mannes, D., Niemz, P., Stähli, P., Kaestner, A., Groso, A.,
373 Stampanoni, M., 2007. 3D imaging of microstructure of spruce wood. *J. Struct. Biol.* 159,
374 46-55.

375 Van den Bulcke, J., Boone, M., Van Acker, J., Van Hoorebeke, L., 2009. Three-Dimensional X-
376 Ray Imaging and Analysis of Fungi on and in Wood. *Microscopy and Microanalysis* 15:
377 395-402.

378 Van den Bulcke, J., Masschaele, B., Dierick, M., Van Acker, J., Stevens, M., Hoorebeke, L.V.,
379 2008. Three-dimensional imaging and analysis of infested coated wood with X-ray
380 submicron CT. *International Biodeterioration & Biodegradation* 61: 278-286.

Figure s (original size)

Dieser Text ist in Times New Roman 12
 Dieser Text ist in Times New Roman 10

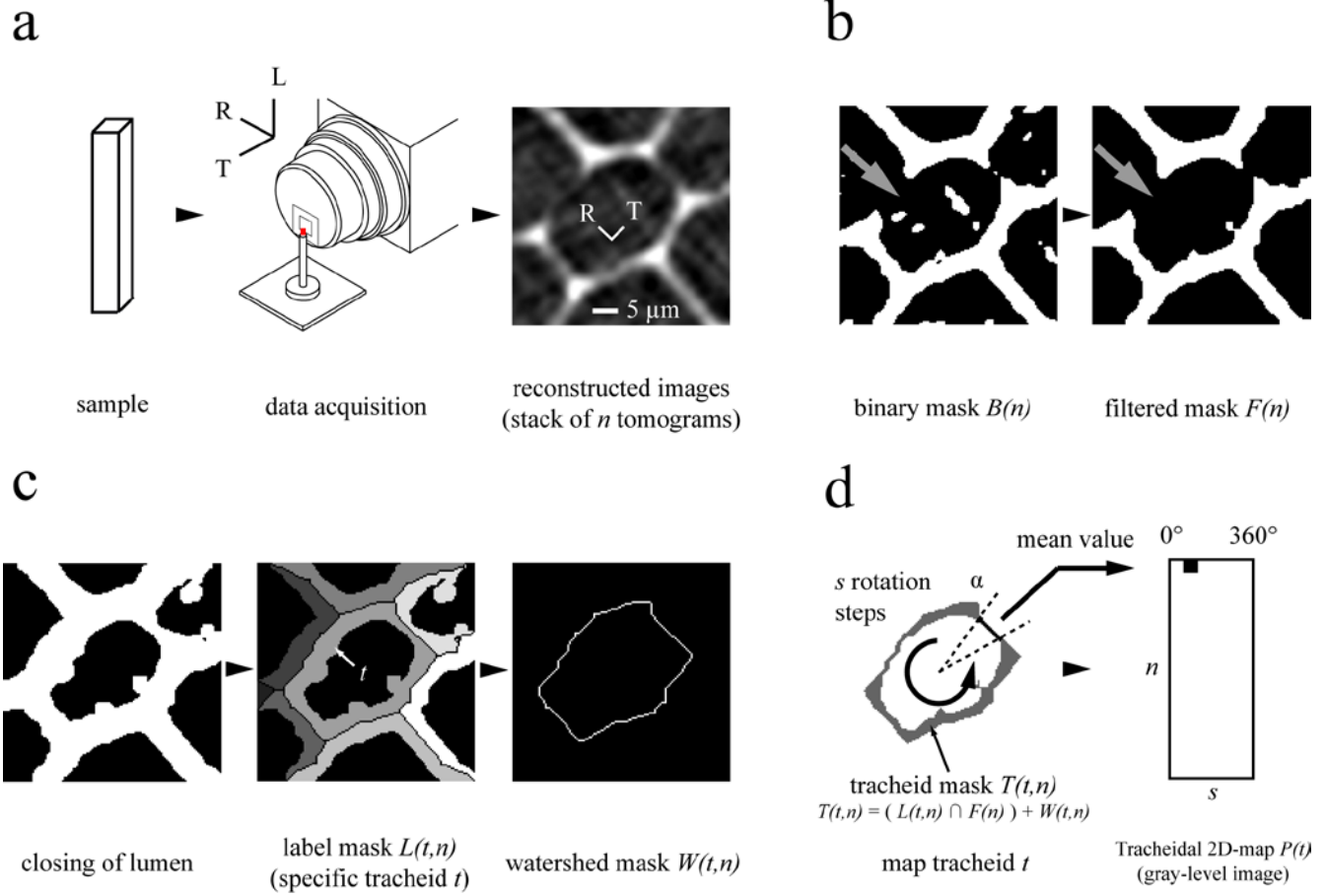


fig1_fullpagewidth_180_125_mm_300dpi.tif

```

1  program Size_Distribution
2  #Read Data
3  I <- Read Stack of n Tomograms
4  Ic <- Crop ROI of I
5
6  #Construction 2D Map
7  for i to n do
8      B <- Compute binary mask of Ic(n)
9      Bc <- Morphological closing of B
10     F(n) <- Remove objects < p pixels from Bc
11 end Return Filtered mask (F)
12
13 Fc <- Morphological closing of F
14 for i to n do
15     S <- Compute skeleton of Fc(n)
16     Sr <- Remove spur pixels from S
17     L(n) <- Compute label mask from Sr and Fc
18 end Return Label mask L
19
20 t <- Choose specific tracheid
21 for i to n do
22     L(t,n) <- Find all pixels of tracheid t in L(n)
23     W(t,n) <- Compute watershed of tracheid t
24     Compute tracheid mask  $T(t,n) = ( L(t,n) \cap F(n) ) + W(t,n)$ 
25     P(t,n) <- Normal cylindric projection P(t,n)
26 end Return Normal cylindrical projection P(t)
27
28 #Size distribution
29 Pb(t) <- Construct binary image of P(t)
30 Compute size distribution of cell wall elements in Pb(t)
31 end program Size_Distribution

```

fig2_onehalfcolumn_170_130_mm.eps

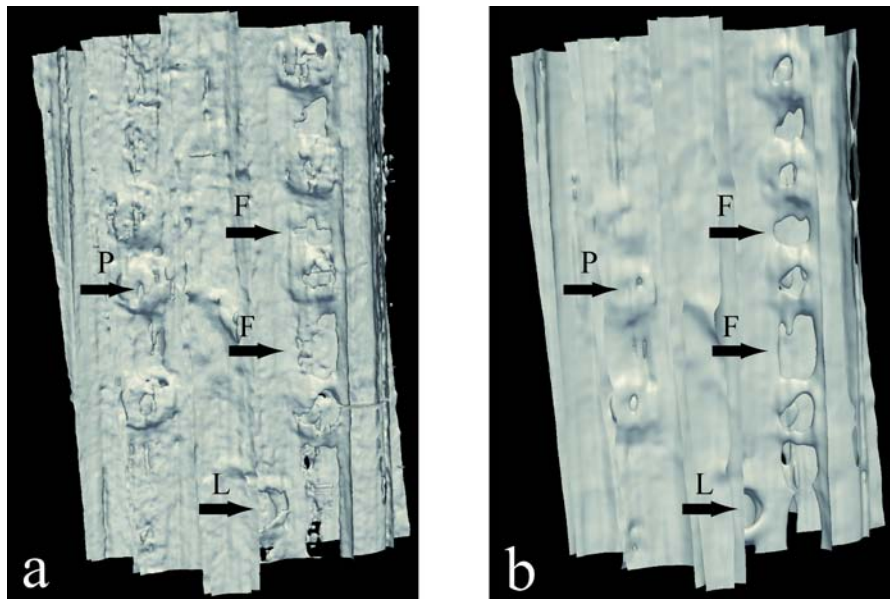


fig3_onehalfcolumn_180_80_mm.tif

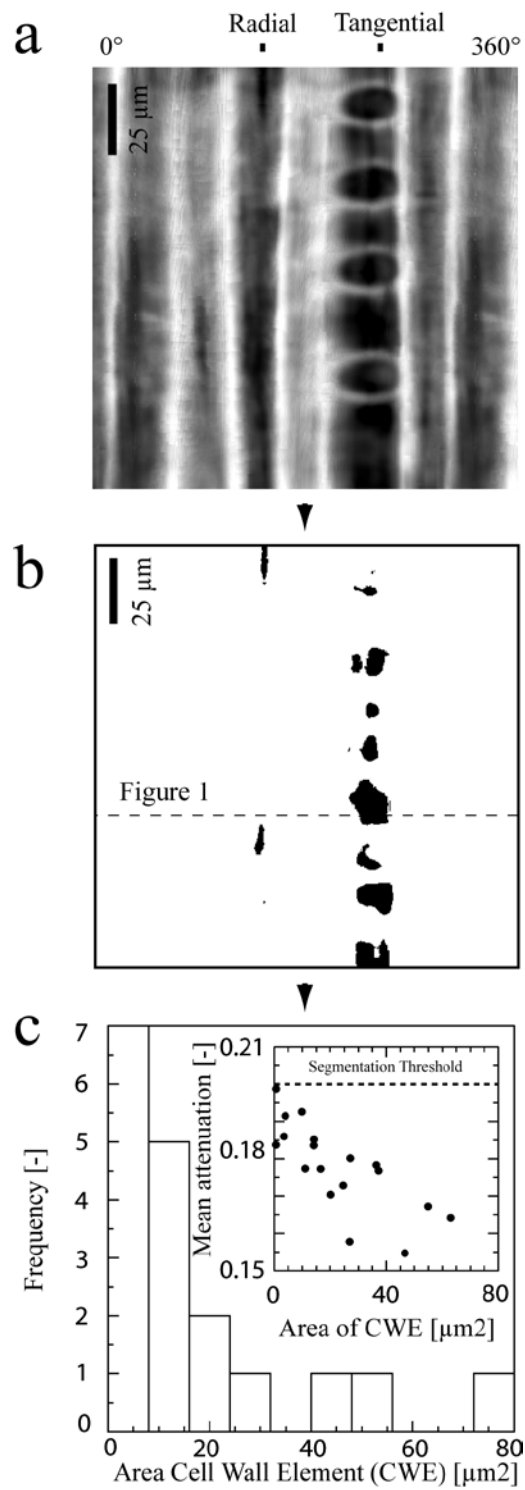


fig4_onecolumnne_70_200_mm.tif